Ground state selection in XY pyrochlore antiferromagnets $R_2Ge_2O_7$ (R = Er, Yb)

Z. L. Dun,[1] X. Li,[2] R. S. Freitas,[3] E. Arrighi,[3] C. R. Dela Cruz,[4] M. Lee,[5,6] E. S. Choi,[6]
H. B. Cao,[4] H. J. Silverstein,[7] C. R. Wiebe,[6,7,8,9] J. G. Cheng,[2] and H. D. Zhou[1,6]

[1]*Department of Physics and Astronomy, University of Tennessee, Knoxville, Tennessee 37996-1200, USA*
[2]*Beijing National Laboratory for Condensed Matter Physics,*
and Institute of Physics, Chinese Academy of Sciences, Beijing 100190, China
[3]*Instituto de Fisica, Universidade de Sao Paulo, CP 66318, 05314-970, Sao Paulo, SP, Brazil*
[4]*Quantum Condensed Matter Division, Oak Ridge National Laboratory, Oak Ridge, Tennessee 37381, USA*
[5]*Department of Physics, Florida State University, Tallahassee, FL 32306-3016, USA*
[6]*National High Magnetic Field Laboratory, Florida State University, Tallahassee, FL 32310-3706, USA*
[7]*Department of Chemistry, University of Manitoba, Winnipeg, MB R3T 2N2 Canada*
[8]*Department of Chemistry, University of Winnipeg, Winnipeg, MB, R3B 2E9 Canada*
[9]*Canadian Institute for Advanced Research, Toronto, Ontario, M5G 1Z7, Canada*
(Dated: August 21, 2015)

Elastic neutron scattering, ac susceptibility, and specific heat experiments on the pyrochlores $Er_2Ge_2O_7$ and $Yb_2Ge_2O_7$ show that both systems are antiferromagnetically ordered in the Γ_5 manifold. The ground state is a ψ_3 phase for the Er sample and a ψ_2 or ψ_3 phase for the Yb sample, which suggests "Order by Disorder"(ObD) physics. Furthermore, we unify the various magnetic ground states of all known $R_2B_2O_7$ (R = Er, Yb, B = Sn, Ti, Ge) compounds through the enlarged XY type exchange interaction $J_\pm$ under chemical pressure. The mechanism for this evolution is discussed in terms of the phase diagram proposed in the theoretical study [Wong et al., Phys. Rev. B 88, 144402, (2013)].

PACS numbers: 75.10.Jm, 61.05.fm, 75.40.-s

The pyrochlores $R_2B_2O_7$ (R: rare earth elements, B: transition metals) have been a hot topic due to their emergent physical properties based on the geometrically frustrated lattice [1, 2]. Recent interest in pyrochlores is focused on systems with effective spin-1/2 R^{3+} ions [3, 4], in which the crystal electric field (CEF) normally introduces a well-isolated Kramers doublet ground state with easy XY planar anisotropy [5, 6]. In these XY pyrochlores, the anisotropic nearest neighbor exchange interaction $J_{ex} = (J_{zz}, J_\pm, J_{z\pm}, J_{\pm\pm})$ between the R^{3+} ions, plus the strong quantum spin fluctuations of the effective spin-1/2 moment, stabilize various exotic magnetic ground states [3].

$Er_2Ti_2O_7$ and $Yb_2Ti_2O_7$ are two celebrated examples of the effective spin-1/2 XY pyrochlores. For $Yb_2Ti_2O_7$, the local [111] Ising-like exchange interaction J_{zz} is considerably larger than the XY planar interaction $J_\pm$ [7]. An unconventional first order transition is observed [8], which has been proposed to be a splayed-ferromagnet (SF) state with Yb^{3+} spins pointing along one of the global major axes with a canting angle [9]. Slight disorder between the Yb and Ti sites leads to a possible quantum spin liquid state [10, 11]. For $Er_2Ti_2O_7$, the Er^{3+} spins are energetically favored to lie within the local XY plane due to the dominating $J_\pm$, in which a continuous U(1) symmetry is preserved in the Hamiltonian that allows the Er^{3+} spins to rotate continuously in the XY plane [12–14]. Recently, both experimental and theoretical studies suggest that the quantum spin fluctuations lift the U(1) degeneracy with a small gap opening in the spin-wave spectrum and select an anti-

ferromagnetic (AFM) ordering state (ψ_2) as the ground state for $Er_2Ti_2O_7$. This is the so called "order by disorder" (ObD) mechanism [14–18], in which the ground state is selected through entropic effects. Meanwhile, an alternative CEF-induced energetic selection mechanism is proposed that will likewise result in the ψ_2 state with similar value of the gap[19, 20].

These delicate magnetic ground states are fragile and easily affected by perturbations, such as chemical pressure. By replacing the Ti^{4+} sites with the nonmagnetic Sn^{4+} and Ge^{4+} ions, the lattice parameter varies to changes the exchange interactions. As listed in Table I, for both $Er_2B_2O_7$ and $Yb_2B_2O_7$ series, the Curie temperature and ordering temperature increase with decreasing lattice parameter. Moreover, their magnetic ground states are markedly different. $Er_2Sn_2O_7$ does not show any long-range magnetic ordering down to 50 mK [21] but displays a spin freezing below 200 mK with the AFM Palmer-Chalker (PC) correlations [22]. It's proposed that $Er_2Sn_2O_7$ is approaching the ψ_2/PC phase boundary where the selection of either state is weak [22–24]. $Er_2Ge_2O_7$ shows an AFM ordering[25] that is similar to $Er_2Ti_2O_7$. While a similar SF phase is observed for both $Yb_2Ti_2O_7$ and $Yb_2Sn_2O_7$ [26–28], $Yb_2Ge_2O_7$ strikingly displays AFM ordering at $T_N = 0.61$ K [29]. So far, the exact nature of the magnetic ground states of $Er_2Ge_2O_7$ and $Yb_2Ge_2O_7$ are not clear. Are they also selected by ObD mechanism? More importantly, while the theoretical studies [3, 23, 24] have made significant efforts to unify the magnetic properties of Yb and Er-XY pyrochlores, unified magnetic phase diagrams have

TABLE I: Comparison between $Er_2B_2O_7$ and $Yb_2B_2O_7$.

	$Er_2B_2O_7$			$Yb_2B_2O_7$		
B site ion	Sn	Ti	Ge	Sn	Ti	Ge
$IR(B^{4+})$(Å)	0.69	0.605	0.53	0.69	0.605	0.53
a(Å)	10.35	10.07	9.88	10.28	10.03	9.83
θ_{CW}(K)	-14	-15.9	-21.9	0.53	0.75	0.9
T_N	$\sim$	1.17	1.41	0.15	0.24	0.62
Order type	$\sim$(AFM)	AFM	AFM	FM	FM	AFM
Reference	[22]	[30]	[25]	[26]	[8]	[29]
Spin state	$\sim$(PC)	ψ_2	ψ_3	SF	SF	$\psi_{2(or3)}$
Reference	[22]	[15]	this work	[26]	[9]	this work

not been experimentally achieved.

In this letter, we studied the polycrystalline pyrochlores $Er_2Ge_2O_7$ and $Yb_2Ge_2O_7$ using elastic neutron scattering under magnetic fields, ac susceptibility, and specific heat measurements. We identified a ψ_3 phase for the Er sample and a ψ_2 or ψ_3 phase for the Yb sample (see Fig. 1 (e)(f) for their spin configurations), which suggest ObD mechanism. Furthermore, we unified the various magnetic ground states of all studied $R_2B_2O_7$ (R = Er, Yb, B = Sn, Ti, Ge) through the enlarged XY type exchange interaction $J_\pm$ under chemical pressure. We discussed this general rule in terms of the phase diagram proposed by Wong et al [24].

Experimental details are listed in the supplemental materials. By comparing the neutron diffraction patterns measured at 3 K and 0.3 K (Fig. 1(a, b)) for $Er_2Ge_2O_7$, several magnetic Bragg peaks, such as (111) (220) (311), etc., are clearly observed at 0.3 K ($< T_N$ = 1.41 K). The refinements using the XY type AFM spin structure in the Γ_5 manifold, either ψ_2 or ψ_3 (Fig. 1(e, f)), fit these magnetic Bragg peaks well with a magnetic moment of 3.23(6) μ_B. In fact, all magnetic phases within the Γ_5 manifold result in the same diffraction pattern and it's impossible to distinguish them in powder samples with zero-field data. Fig .1(d) shows the field dependence of the (220) and (311) Bragg peaks' intensities. The details are: (i) with H < 0.15 T, a magnetic domain alignment results in a quick drop of the (220) peak intensity with increasing field; (ii) between 0.15 and 2 T, the spins gradually rotates with the magnetic field but keeps the AFM nature; (iii) around a critical field H_c = 2 T, the (220) Bragg peak's intensity abruptly drops to a background value while the (311) Bragg peak's intensity continuously increases. This demonstrates that above H_c, $Er_2Ge_2O_7$ enters a spin polarized state. The observed FM (400) and AFM (200) Bragg peaks on the pattern measured at H = 5 T (Fig. 1(c)) suggest that this polarized state is similar to the SF state in the Γ_9 manifold. The refinement by assuming one single SF structure with the magnetic field applied along the global z axis (Fig .1(g))actually fits the powder average 5 T data well with the Er^{3+} moment as $\vec{M}$=($\pm$1.42(2), $\pm$1.42(2), 4.40(1)) μ_B in the global coordinate frame. The double peak feature of the reported ac
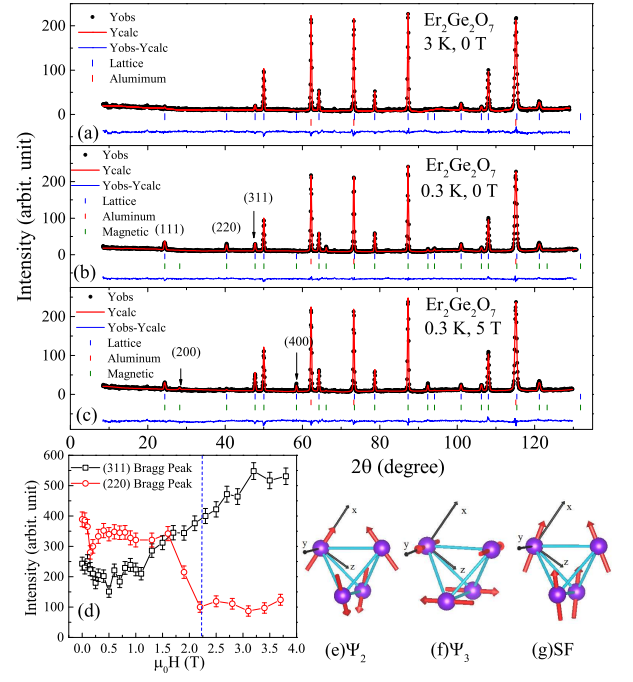

FIG. 1: (color online) Elastic neutron scattering patterns and Rietveld refinements for $Er_2Ge_2O_7$ at (a)T = 3 K and H = 0 T, (b)T = 0.3 K and H = 0 T, and (c)T = 0.3 K and H = 5 T. (d) The field dependence of the (200) and (311) Bragg Peaks' intensities measured at T = 0.3 K, the critical field H_c is marked as the dash line. The spin configurations for (e)ψ_2, (f)ψ_3 and (g)splayed-ferromagnetic (SF) phases in the local coordination.

susceptiblity data for $Er_2Ge_2O_7$ also confirmed the magnetic domain alignment around 0.15 T and the critical field around 2 T [25].

It has been pointed out [15] that (i)for both ψ_2 and ψ_3 states, a multi-domain state with equal fraction of 6 magnetic domains (plotted in the supporting material) at zero field will be expected, which give different intensities of the (220) Bragg peak; (ii)with the applied magnetic field in [1$\bar{1}$0] direction, two domains with larger intensity will be selected if the ψ_2 phase is present [14, 31]. This will result in a (220) peak's intensity jump, which has been exactly observed for $Er_2Ti_2O_7$ in the single crystal neutron diffraction experiments [14, 31]; (iii)similarly, if the ψ_3 state is selected, a decrease is expected for the (220) peak's intensity since the two domains with lower intensities will be selected. In our neutron powder diffraction experiment by using a pelleted sample, the magnetic field was applied vertically such that it is perpendicular to the scattering plane. Then a similar selection rule would be expected in addition to a powder averaging effect (see detailed analysis in the supporting material). As shown in Fig. 1(d), the (220) peak's intensity drops dramatically from 400 at 0 T to 250 counts at 0.15 T. This result suggests that $Er_2Ge_2O_7$ orders in the ψ_3 phase. However, in order to provide unambiguous
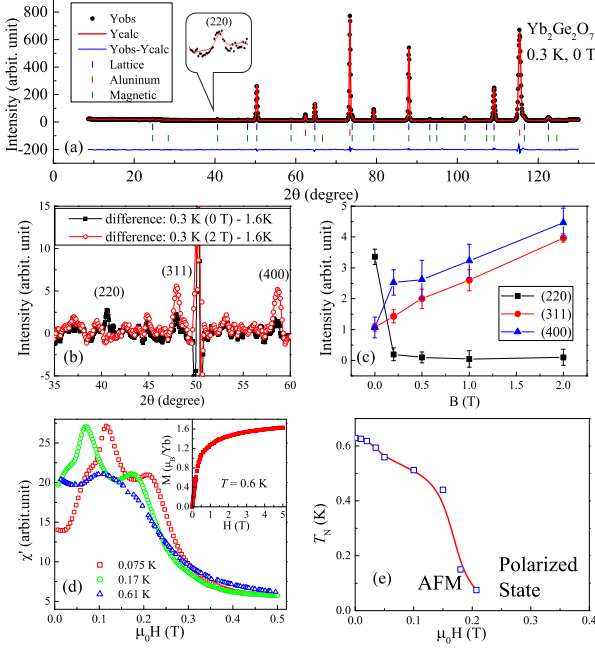
FIG. 2: (color online) (a)Elastic neutron scattering pattern and Rietvelt refinement for $Yb_2Ge_2O_7$ at $T = 0.3$ K and H = 0 T. (b) The difference between the patterns measured at 0.3 K (with H = 0 and 2 T) and 1.6 K. (c) The field dependence of the (200), (311) and (400) Bragg Peaks' intensities at 0.3 K. (d) The ac susceptibility of $Yb_2Ge_2O_7$ at different temperatures. Insert: the dc magnetization measured at 0.6 K. (e) The magnetic phase diagram of $Yb_2Ge_2O_7$.

evidences for the ψ_3 state, polarized neutron experiments on a single crystal sample are needed.

Fig. 2(a) shows the neutron diffraction pattern measured at 0.3 K ($< T_N = 0.62$ K) for $Yb_2Ge_2O_7$. Due to the small magnetic moment of the Yb^{3+} ions, the magnetic Bragg peaks are weak (as shown in the insert). The difference between the 0.3 K and 1.6 K patterns (Fig. 2(b)) more clearly shows that the observed magnetic Bragg peaks' positions and intensity ratios are very similar to those of $Er_2Ge_2O_7$, which identifies $Yb_2Ge_2O_7$'s ground state as either ψ_2 or ψ_3 in the Γ_5 manifold. Refinements based on these two spin structures give the same Yb^{3+} moment of 1.06(7) μ_B, which is consistent with the previous report ($Yb^{3+} \approx 1.15\ \mu_B$) [32].

With an applied magnetic field on $Yb_2Ge_2O_7$ (Fig. 2(c), the (220) peak's intensity decreases quickly around 0.2 T, which indicates a critical field $H_c \sim 0.2$ T. Upon H_c, the (311), (400) magnetic Bragg peaks experience a continuous increase, showing a continuous polarization of Yb^{3+} spin towards the direction of the magnetic field. The refinement of the 0.3 K pattern measured under 2 T actually yields a SF state with $\vec{M}$=($\pm$0.31(5), $\pm$0.31(5), 1.57(9))μ_B in the global coordinate frame. The critical field is also confirmed by the ac magnetization measurement (Fig. 2(d)). At 75 mK, the ac susceptibility first
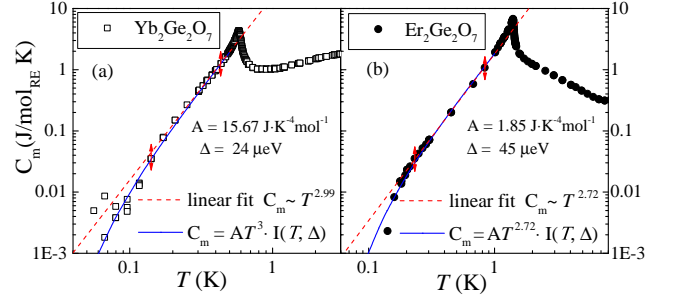
shows a peak at 0.12 T due to the domain alignment, and then another peak around $H_c = 0.22$ T to enter the polarized state. With increasing temperature, both peaks' positions move to lower fields and finally disappear above T_N. This double peak feature is similar to that of $Er_2Ge_2O_7$[25]. Along with our previous reported ac susceptibility data on $Yb_2Ge_2O_7$[29], a magnetic phase diagram is plotted in Fig. 2(e). However, due to the weak magnetic signal at (220) and the small H_c, it's difficult to study how exactly this domain alignment affects the (220) peak's intensity, which obstructs us to distinguish between ψ_2 and ψ_3. One noteworthy feature is that the dc magnetization measured at 0.6 K for $Yb_2Ge_2O_7$ reaches 1.6 μ_B at 5 T. This value is consistent with that of $Yb_2Ti_2O_7$ and confirms the similar CEF scheme between the Ge and Ti samples [32].

The selection of either ψ_2 or ψ_3 phase breaks the continuous U(1) symmetry, which requires a pseudo-Goldstone mode with a small spin-wave gap below T_N. For $Er_2Ti_2O_7$, the inelastic neutron scattering has confirmed the existence of this gap ($\sim 50\ \mu$eV) [18]. Meanwhile, the specific heat data can reveal the information of this gap. Fig. 3(a) shows the electronic magnetic specific heat (C_m) of $Yb_2Ge_2O_7$ (details about obtaining C_m are listed in the supplemental materials). Below T_N, C_m follows an almost prefect T^3 behavior down to 0.2 K, as the red dash line shows. However, it's obvious that C_m deviates from this straight T^3 line to a lower value below 0.2 K. Contrasting to a Goldstone mode where the C_m strictly follows a T^3 law, the gap that exists in the pseudo-Goldstone mode will multiply a component $I_\Delta(T)$ to T^3, which is temperature dependent only in the temperature region that is comparable to the energy gap Δ. The relationship between the C_m and Δ has already been derived in the supporting material of Ref. [14]. Here we

FIG. 3: (color online) The electronic magnetic specific heat C_m for (a)$Yb_2Ge_2O_7$ and (b)$Er_2Ge_2O_7$. The red dash lines show linear fits of the arrow-marked regions and the blue solid lines show fits considering the spin-wave gap.

rewrite it as:

$$C_m^\Delta = \frac{\mathcal{N}_A k_B^4 \pi^2 a^3}{120 \overline{v}^3} \left(\frac{15}{16 \pi^4} \int_0^\infty dX \frac{X^2 \left(X^2 + \delta^2\right)}{\sinh^2 \frac{\sqrt{X^2+\delta^2}}{2}} \right) T^3$$

$$= A \, I_\Delta(T) \, T^3 \qquad (1)$$

where $\mathcal{N}_A$ is the Avogadro constant, k_B is the Boltzmann constant, a is the lattice constant, $\overline{v}$ is the geometric mean of magnon velocity, $X = \beta \tilde{k}$ and $\delta = \beta \Delta$ (dimensionless). The integration $I_\Delta(T)$ can be evaluated numerically with a given Δ. $I_\Delta(T)$ approaches a unity at high temperatures but decreases quickly when $k_B T$ is comparable to Δ, which leads the deviation of the C_m^Δ from the T^3 behavior at low temperatures. The best fit of the measured C_m to Eq. 1 with the Δ and A as two variables (blue line in Fig. 3(a)) yields the $\Delta = 24$ μeV and $A = 15.67$ J.K^{-4}mol^{-1}, which corresponds to $\overline{v} = 45.8$ m/s.

Similar analysis of the C_m for Er$_2$Ge$_2$O$_7$ (Fig. 3(b)) yields a spin-wave gap $\Delta = 45$ μeV with $A = 1.85$ J.K^{-4}mol^{-1}(corresponds to $\overline{v} = 132$ m/s). One noticed feature is that at high temperatures, C_m follows a $T^{2.72}$ (not strict T^3) behavior. This could be due to the error bar introduced by the low temperature nuclear Schottky anomaly subtraction.

With the decreasing lattice parameter or the increasing chemical pressure through the Sn to Ti to Ge samples, the magnetic ground states change accordingly (Table I). Given the fact that in these XY pyrochlores, the J_{ex} dominate the magnetic properties, the chemical pressure can finely tune the J_{ex} to lead to various magnetic ground states. This change of J_{ex} is supported by the systematic changes of the Curie temperature and ordering temperature for XY-pyrochlores listed in Table I. Most strikingly, this is the first time to experimentally confirm an AFM $\psi_{2 \ or \ 3}$ phase in Yb-pyrochlores despite the apparently different dominant exchange interactions between Yb and Er-pyrochlores(Ising-like J_{zz} for Yb-pyrochlores and the XY-planar $J_\pm$ for Er-pyrochlores). This finding indicates there is general rules to unify the various magnetic ground states of all effective spin-1/2 pyrochlores.

Recent theoretical studies have made significant efforts to unify the magnetic ground states of the XY-pyrochlores. Wong et al. [24] have scaled the J_{ex} by $J_\pm$ as three variables($J_{zz}/J_\pm$, $J_{z\pm}/J_\pm$, $J_{\pm\pm}/J_\pm$) and calculated a two dimensional magnetic phase diagram with the fixed ratio of $J_{zz}/J_\pm$, which contains continuous phase boundaries among the PC, SF, ψ_2 and ψ_3 phases (the selection between ψ_2 and ψ_3 phases is through ObD). By comparing to the exchange interaction values obtained from the inelastic neutron scattering measurements, they successfully located the two Ti samples ($J_{zz}/J_\pm \approx$ -0.5, $J_{z\pm}/J_\pm \approx 0$, $J_{\pm\pm}/J_\pm \approx 1.0$ for Er$_2$Ti$_2$O$_7$ and $J_{zz}/J_\pm \approx$ 3.0, $J_{z\pm}/J_\pm \approx$ -2.7, $J_{\pm\pm}/J_\pm \approx 1.0$ for Yb$_2$Ti$_2$O$_7$) in the ψ_2 and SF phase, respectively. Although we are short of knowledge of the exchange interaction values of other

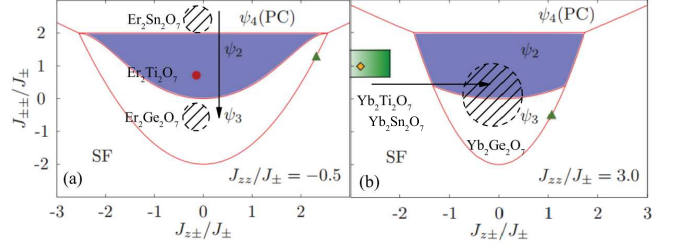FIG. 4: (color online) Magnetic ground state phase diagrams for (a)Er$_2$B$_2$O$_7$ series and (b)Yb$_2$B$_2$O$_7$ series adopted from Ref. [24]. The dash areas are for just for the illustration purpose. The trends for the chemical pressure effects are shown as the direction of the arrows.

XY-pyrochlores, here we located them in the $J_{zz}/J_\pm =$ -0.5 and the $J_{zz}/J_\pm = 3.0$ phase diagrams adopted from Ref. [24]. This is based on two facts: (i) the phase diagram areas and boundaries are similar to each other over a wide range value of $J_{zz}/J_\pm$; (ii) the chemical pressure can finely tune but may not dramatically affect the ratio of $J_{zz}/J_\pm$. As shown in Fig. 4, with increasing chemical pressure, two general trends are obvious: (i) the ground state moves downwards from PC state in Er$_2$Sn$_2$O$_7$ to ψ_2 in Er$_2$Ti$_2$O$_7$ and then ψ_3 in Er$_2$Ge$_2$O$_7$ for the Er-pyrochlores in the $J_{zz}/J_\pm =$ -0.5 phase diagram; (ii) the grounds states move rightwards from the SF state of Yb$_2$Ti$_2$O$_7$ to the ψ_2 or ψ_3 region of Yb$_2$Ge$_2$O$_7$ in the $J_{zz}/J_\pm = 3.0$ phase diagram.

These two trends can be successfully unified by the scenario that the increasing chemical pressure enhances $J_\pm$. For Er-pyrochlores with dominant XY type interactions, J_{zz} and $J_{z\pm}$ will take small values. Therefore, the increasing $J_\pm$ will primarily decrease the ratio of $J_{\pm\pm}/J_\pm$ to result in a downwards movement of the ground state. On the other hand, for Yb-pyrochlores with dominant local [111] Ising like interactions, $J_\pm$ and $J_{\pm\pm}$ will take small values. Therefore, the increasing $J_\pm$ will mainly decrease the ratio of $J_{z\pm}/J_\pm$ to result in a rightwards shift of the ground state to reach the AFM state for Yb$_2$Ge$_2$O$_7$. Although without the values of the exchange interactions for all XY-pyrochlores, we cannot conclude the increase of the $J_\pm$ as the only reason for the change of ground states, the comparison between the reported $J_\pm$ values of Er$_2$Sn$_2$O$_7$($J_\pm = 1.35$ meV)[22] and Er$_2$Ti$_2$O$_7$ ($J_\pm = 6.7$ meV) [14] supports our proposed scenario.

Similar to Er$_2$Ti$_2$O$_7$, the debate arises over what is the microscopic mechanism that breaks the continuous U(1) symmetry and selected the ordered phase below T_N. For the ObD scenario, the selection comes from the quantum fluctuations and is delicately tuned by the exchange parameters J_{ex} [14–17](Fig. 4). For the CEF-induced energetic selection scenario considering additional CEF Hamiltonian and dipolar interaction (J_{dip}), the ψ_2 phase is predicted in the Γ_5 manifold [19, 22]. The ψ_3 phase

can only be achieved while adding a relatively strong Dzyaloshinskii-Moriya interaction (J_{DM}) [20]. Since the experimental results show that the change of lattice parameter under chemical pressure has larger influences on J_{ex} than CEF, J_{dip} and J_{DM} [29]. The selection of different ground state in $Er_2Ti_2O_7(\psi_2)$ and $Er_2Ge_2O_7(\psi_3)$ seems to favor the ObD scenario. Furthermore, it is noticed that the values of magnon mean velocity and the gap in $Yb_2Ge_2O_7$ ($\overline{v} = 45.8$ m/s, $\Delta = 24$ μeV) are both smaller than that of $Er_2Ge_2O_7$ ($\overline{v} = 132$ m/s, $\Delta = 45$ μeV), which is consistent with the ObD mechanism. A smaller $\overline{v}$ suggests a softer low lying mode in the spin wave spectrum that will result in a smaller energy difference of spin-wave spectrum between the ψ_2 and ψ_3 phases[14], for which a smaller gap value is expected.

———————

[1] J. S. Gardner, M. J. P. Gingras and J. E. Greedan, Rev. Mod. Phys. **82**, 53 (2010).
[2] L. Balents, Nature **464**, 08917 (2010).
[3] L. Savary and L. Balents, Phys. Rev. Lett., **108**, 037202 (2012).
[4] S. Onoda, J. Phys.: Conf. Series bf 320, 012065 (2011).
[5] J. D. M. Champion and P. C. W. Holdsworth, J. Phys.: Condens. Matter **16**, S665 (2004).
[6] H. B. Cao, A. Gukasov, I. Mirebeau, P. Bonville, C. Decorse, G. Dhalenne, Phys. Rev. Lett., **103**, 056402 (2009).
[7] K. A. Ross, L. Savary, B. D. Gaulin, and L. Balents, Phys. Rev. X **1**, 021002 (2011).
[8] J. A. Hodges, P. Bonville, A. Forget, A. Yaouanc, P. Dalmas de Reotier, G. Andre, M. Rams, K. Krolas, C. Ritter, P. C. M. Gubbens, C. T. Kaiser, P. J. C. King and C. Baines, Phys. Rev. Lett. **88**, 077204 (2002).
[9] L. J. Chang, S. Onoda, Y. Su, Y. J. Kao, K. D. Tsuei, Y. Yasui, K. Kakurai and M .R. Lees, Nat. Commun. **3**, 992 (2012).
[10] K. A. Ross, J. P. C. Ruff, C. P. Adams, J. S. Gardner, H. A. Dabkowska, Y. Qiu, J. R. D. Copley and B. D. Gaulin, Phys. Rev. Lett. **103**, 227202 (2009).
[11] K. A. Ross, T. Proffen, H. A. Dabkowska, J. A. Quilliam, L. R. Yaraskavitch, J. B. Kycia and B. D. Gaulin, Phys. Rev. B, **86**, 174424 (2012).
[12] J. D. M. Champion, M. J. Harris, P. C. W. Holdsworth, A. S. Wills, G. Balakrishnan, S. T. Bramwell, E. Cizmar, T. Fennell, J. S. Gardner, J. Lago, D. F. McMorrow, M. Orendac, A. Orendacova, D. M. Paul, R. I. Smith, M. T. F. Telling and A. Wildes, Phys. Rev. B **68**, 020401(2003).
[13] J. P. C. Ruff, J. P. Clancy, A. Bourque, M. A. White, M. Ramazanoglu, J. S. Gardner, Y. Qiu, J. R. D. Copley, M. B. Johnson, H. A. Dabkowska and B. D. Gaulin, Phys. Rev. Lett. **101**, 147205 (2008).
[14] L.Savary, K. A. Ross, B. D. Gaulin, J. P. C. Ruff and Leon Balents, Phys. Rev. Lett. **109**, 167201 (2012).
[15] A. Poole, A. S. Wills and E. E. Lelievre-Berna, J. Phys.: Condens. Matter **19**, 452201 (2007).
[16] P. A. McClarty, P. Stasiak and M. J. P. Gingras, Phys. Rev. B, **89**, 024425 (2014).
[17] M. E. Zhitomirsky, M. V. Gvozdikova, P. C. W. Holdsworth and R. Moessner, Phys. Rev. Lett. **109**, 077204 (2012).
[18] K. A. Ross, Y. Qiu, J. R. D. Copley, H. A. Dabkowska and B. D. Gaulin, Phys. Rev. Lett., **112**, 057201 (2014).
[19] S. Petit, J. Robert, S. Guitteny, P. Bonville, C. Decorse, J. Ollivier, H. Mutka, M. J. P. Gingras and I. Mirebeau, Phys. Rev. B, **90**, 060410(R) (2014).
[20] P. A. Mcclarty, S. H Curnoe and M. J. P. Gingras, J. Phys. : Conf. Ser. **145**, 012032 (2009).
[21] P. M. Sarte, H. J. Silverstein, B. T. K. Van Wyk, J. S. Gardner, Y. Qiu, H. D. Zhou and C. R. Wiebe, J. Phys.: Condens. Matter **23**, 382201 (2011).
[22] S. Guitteny, S. Petit, E. Lhotel, J. Robert, P. Bonville, A. Forget, and I. Mirebeau, Phys. Rev. B, **88**, 134408 (2013).
[23] H. Yan, O. Benton, L. D. Jaubert, and N. Shannon, arXiv:1311.3501.
[24] A. W. C. Wong, Z. Hao, and M. J. P. Gingras, Phys. Rev. B, **88**, 144402 (2013).
[25] X. Li, W. M. Li, K. Matsubayashi, Y. Sato, C. Q. Jin, Y. Uwatoko, T. Kawae, A. M. Hallas, C. R. Wiebe, A. M. Arevalo-Lopez, J. P. Attfield, J. S. Gardner, R. S. Freitas, H. D. Zhou, and J.-G. Cheng, Phys. Rev. B **89**, 064409 (2014).
[26] A. Yaouanc, P. Dalmas de Reotier, P. Bonville, J. A. Hodges, V. Glazkov, L. Keller, V. Sikolenko, M. Bartkowiak, A. Amato, C. Baines, P. J. C. King, P. C. M. Gubbens, and A. Forget, Phys. Rev. Lett. **110**, 127207 (2013).
[27] Z. L. Dun, E. S. Choi, H. D. Zhou, A. M. Hallas, H. J. Silverstein, Y. Qiu, J. R. D. Copley, J. S. Gardner, and C. R. Wiebe, Phys. Rev. B **87**, 134408 (2013).
[28] J. Lago, I. Zivkovic, J. O. Piatek, P. Alvarez, D. Huvonen, F. L. Pratt, M. Diaz, T. Rojo, Phys. Rev. B **89**, 024421 (2014).
[29] Z. L. Dun, M. Lee, E. S. Choi, A. M. Hallas, C. R. Wiebe, J. S. Gardner, E. Arrighi, R. S. Freitas, A. M. Arevalo-Lopez, J. P. Attfield, H. D. Zhou and J. G. Cheng, Phys. Rev. B **89**, 064401 (2014).
[30] P. D. Reotier, A. Yaouanc, Y. Chapuis, S. H. Curnoe, B. Grenier, E. Ressouche, C. Marin, J. Lago, C. Baines and S. R. Giblin, Phys. Rev. B **86**, 104424 (2012).
[31] H. B. Cao, I. Mirebeau, A. Gukasov, P. Bonville, C. Decorse, Phys. Rev. B, **82**, 104431 (2010).
[32] J. A. Hodges, P. Bonville, A. Forget, M. Rams, K. Krolas, and G. Dhalenne, J. Phys.: Condens. Matter **13**, 9301 (2001).

Supplemental material

1. EXPERIMENTAL SETUPS

Polycrystalline sample $Er_2Ge_2O_7$ and $Yb_2Ge_2O_7$ were synthesized by the high-pressure and high-temperature (HPHT) technic. Proper ratio of starting materials Yb_2O_3, Er_2O_3, GeO_2 were mixed and synthesized in a Walker-type mutlianvil module (Rockland Research Co.) under 7 GPa and 1300 K. The ac susceptibility was measurements down to 20 mK on a home-made set up at SCM1 of National High Magnetic Field Laboratory. The dc magnetization measurements were performed using a Quantum Design superconducting interference device (SQUID) magnetometer using a magnetic field of 0.01 T. The low temperature specific heat measurements were made in a Dilution Refrigerator option of the Physical Property Measurement System (PPMS, Quantum Design) using a standard semi-adiabatic heat pulse technique. Elastic neutron scattering measurement was performed at Neutron Powder Diffractometer (HB-2A) at High Flux Isotope Reactor(HFIR) in Oak Ridge National Laboratory (ORNL). Neutron wavelength $\lambda = 2.41$ Å was used to maximize low angle magnetic scattering. Lattice and magnetic structure were refined though software package *Fullprof-suite*.

2. MAGNETIC DOMAIN ALIGNMENT IN THE MAGNETIC FIELD

For our powder neutron diffraction experiment on polycrystalline samples of $Er_2Ge_2O_7$ and $Yb_2Ge_2O_7$, there are three main effects under consideration. (i)The grains are randomly oriented in the sample which determine different orientations of the tetrahedrons. (ii)In the Γ_5 manifold, the U(1) rotational symmetry allows the four spins in a tetrahedron to rotate simultaneously in the local XY plane (we notate α as the angle of the spin relatively to the local x-axes in Fig. 1(d)). Then a single α defines an unique set of spin configuration. For a specific ψ_2 or ψ_3 phase, there are six magnetic domains with $\alpha = n\pi/3$ (n = 0,...,5) for the ψ_2 phase and $\alpha = n\pi/3 + \pi/6$ (n = 0,...,5) for the ψ_3 phase. In both cases, the six domains will be equally populated in a zero-field cooled sample below T_N. (iii)For a powder Bragg peak, it's intensity is composed of all equivalent reflections. Specifically for the (220) Bragg peak, its intensity is equally contributed by six equivalent reflections: $\mathbf{q_1}$ = 220, $\mathbf{q_2}$ = 202, $\mathbf{q_3}$ = 022, $\mathbf{q_4}$ = 2$\bar{2}$0, $\mathbf{q_5}$ = 20$\bar{2}$, $\mathbf{q_6}$ = 02$\bar{2}$.

We will begin with reflection of $\mathbf{q_1}$ = 220 and show that the magnetic domain alignment behavior will be the same for all six reflections given a ψ_2 or ψ_3 phase. Namely, all reflections' intensities will increase for a ψ_2 phase and decrease for a ψ_3 phase. Thus the observed (220) Bragg peaks' intensity drop in $Er_2Ge_2O_7$ under a small magnetic field identifies the ψ_3 phase.

Fig. 1(a) illustrates our setup for the neutron powder diffraction experiments. The samples were pressed into pellets, wrapped by aluminum foils and fixed inside an aluminium can during the experiment to prevent mechanical motion of the grains. The magnetic field was applied vertically so that it is perpendicular to the scattering plane. For the $\mathbf{q_1}$ = 220 reflection, its intensity comes from all grains with its [110] direction along $\mathbf{q_1}$. Then the geometry defines a grain-average plane that is perpendicular to $\mathbf{q_1}$ where the magnetic filed direction, all grains' [001] and [1$\bar{1}$0] axes lie within (Fig. 1(b)). Assuming equally distribution of different grains in the powder sample, then the effect of averaging different grains with a unique magnetic field direction in the grain-average plane (the case of the experiment) is equivalent to that of averaging random magnetic field directions to a single grain in a field-average plane (the case for modeling). The resulting ($\bar{h}$hl) field-average plane following the definition of the grain orientation is shown in Fig. 1(c). Its relationship to the Er^{3+} tetrahedron is illustrated in Fig. 1(d).

Fig. 2 shows the magnetic Bragg peaks' intensity as a function of α for all (220) type reflections calculated using the software package *Fullprof-suite*. For the $\mathbf{q_1}$ = 220 reflection, the intensity for the six ψ_2 domains (dots in Fig. 3(a)) will take two large values (for $\alpha = 0$ and π)and four small values (for $\alpha = \pi/3$, $2\pi/3$, $4\pi/3$, $5\pi/3$). With the magnetic field plane defined above for $\mathbf{q_1}$, the $\alpha = 0$ and $\alpha = \pi$ states will be selected by the symmetry as shown in the first row of Fig. 3. Then the intensity of $\mathbf{q_1}$ = 220 reflection will experience an increase due to the magnetic domain alignment under magnetic fields. On the other hand, the intensity for the six ψ_3 domains (square in Fig. 2(a)) will take four large values (for $\alpha = \pi/6$, $5\pi/6$, $7\pi/6$, $11\pi/6$) and two small values (for $\alpha = \pi/2$, $3\pi/2$). The later two spin configurations with small intensities will be selected by symmetry as shown in the bottom row of Fig. 3, resulting the intensity drop for the $\mathbf{q_1}$ = 220 reflection.

The same analysis will apply for other reflections $\mathbf{q_i}$ (i = 2,...,5) which define different magnetic planes (Fig. 1(e-i)) with according magnetic reflection intensities (Fig. 2(b-f)). Take the $\mathbf{q_6}$ = 02$\bar{2}$ for example, the according (lhh) field-average plane (Fig. 1(i)) favors $\alpha = \pi/3$, $4\pi/3$ states for the ψ_2 phase and $\alpha = 5\pi/6$, $11\pi/6$ states for the ψ_3 phase. The resulting intensity change in Fig. 2(f) will be exactly same as the $\mathbf{q_1}$ situation.

In summary, considering the grain population and equivalent reflections effect in the powder sample, the decrease of (220) Bragg peak's intensity due to magnetic domain alignment identifies the ψ_3 phase in $Er_2Ge_2O_7$.
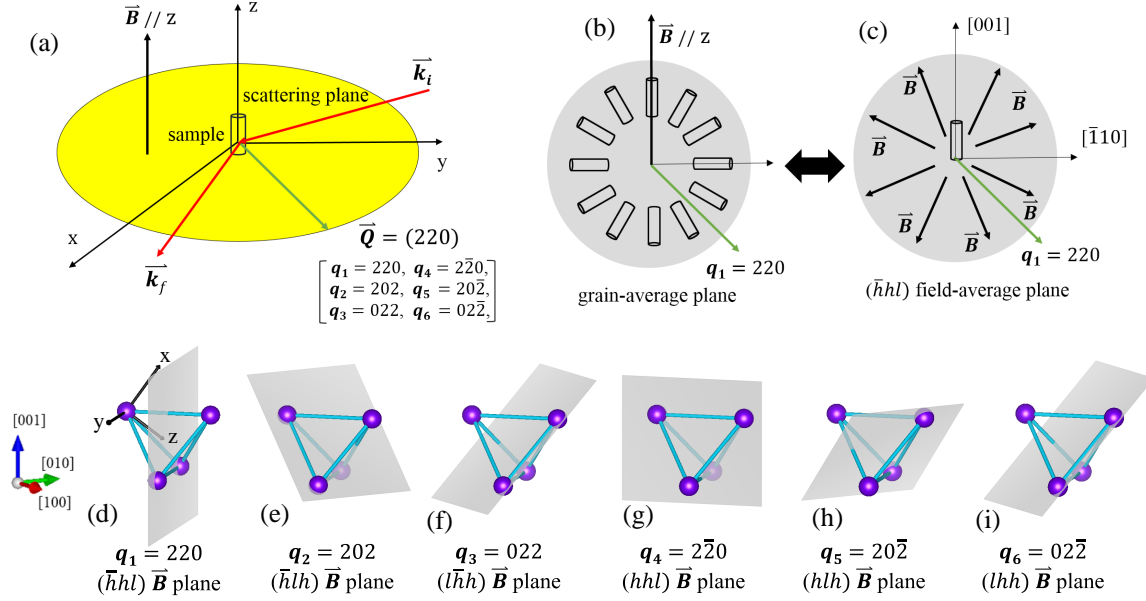
FIG. 5: (a)Experimental setup for the powder neutron diffraction experiment. The six equivalent (220) type reflections are labeled as $\mathbf{q_i}$ (i = 1,...,5). (b)(c)Illustration of the grain-average and the according field-average for a single reflection $\mathbf{q_1}$. (d-i)Different magnetic field-average planes for different $\mathbf{q_i}$.
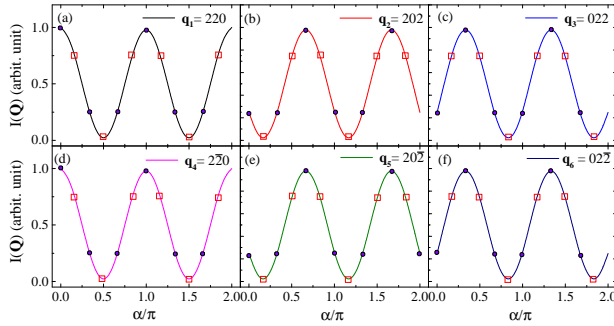

FIG. 6: Magnetic Bragg peak's intensity as a function of rotation angle α for different (220) type reflections. The solids dots represent the six ψ_2 domains and the open squares represent the six ψ_3 domains.

FIG. 7: The six magnetic domains' spin configurations for the ψ_2 and ψ_3 phases. The magnetic field-average plane is illustrated for $\mathbf{q_1} = 220$.

3. ELECTRONIC MAGNETIC CONTRIBUTION TO THE SPECIFIC HEAT

We obtain the electronic magnetic contribution (C_m) to the specific heat for $Er_2Ge_2O_7$ and $Yb_2Ge_2O_7$ after subtracting the lattice (C_L) and magnetic nuclear (C_N) contributions from the total measured specific heat (C_T) of each sample. The lattice contribution was estimated measuring the structurally similar non-magnetic material $Lu_2Ge_2O_7$ (see Fig. 4). The exact expression for the nuclear specific heat is [1]:
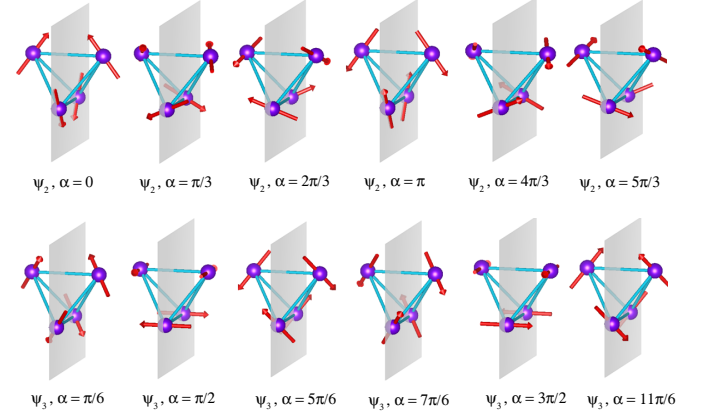
$$C_N = \frac{R}{\left(k_B T\right)^2} \frac{\sum\limits_{i=-I}^{i=I}\sum\limits_{j=-I}^{j=I}\left(W_i^2 - W_i W_j\right)e^{-\frac{W_i+W_j}{k_B T}}}{\sum\limits_{i=-I}^{i=I}\sum\limits_{j=-I}^{j=I}e^{-\frac{W_i+W_j}{k_B T}}} \quad (2)$$
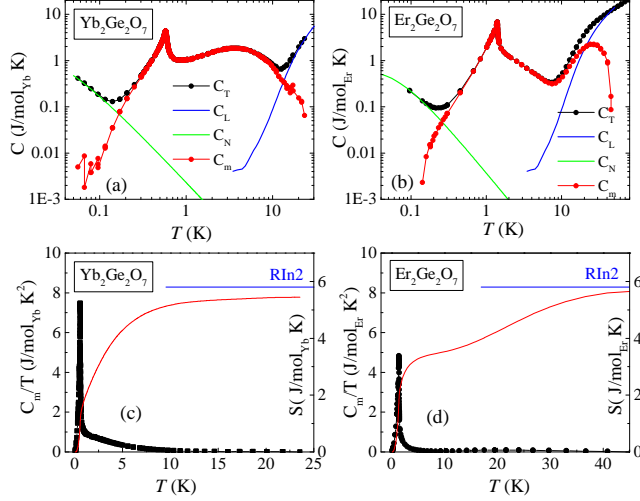
FIG. 8: Total specific heat (C_T) for (a)$Yb_2Ge_2O_7$ and (b) $Er_2Ge_2O_7$. The electronic magnetic contribution (C_m) is obtained after the subtraction of the lattice (C_L) and magnetic nuclear (C_N) specific heat. C_m/T and the integrated entropy for (c)$Yb_2Ge_2O_7$ and (d)$Er_2Ge_2O_7$.

where I is the nuclear spin and the energy levels W_i are given by [1]:

$$\frac{W_i}{k_B} = -a'i + P\left(i^2 - \frac{1}{3I(I+1)}\right) \qquad (3)$$

$$i = -I, -I+1, ..., I-1, I \qquad (4)$$

Here a' $= \mu H_{eff}/k_B I$ and $P = 3e^2Qq/4kI(2I\text{-}1)$ are the magnetic interaction parameter and the quadrupole coupling constant. We use the nuclear spin I of each compound and fit the low temperature part of the data with a' and P as adjustable parameters to obtain the nuclear contribution to the specific heat as shown in Fig. 4(a)(b).

The C_m/T and the integrated magnetic entropy for both samples are plotted in Fig. 4(c)(d). For both samples, the recovered magnetic entropies almost reach Rln2.

[1] O. V. Lounasmaa, A. J. Freeman e R. B. Frankel, "Nuclear specific heats in metals and alloys," in *Hyperfine Interactions*, New York, Academic Press, 1967, pp. 467-496.